

Wicking dynamics in yarns

Robert Fischer^{a,b,c,*}, Christian M. Schlepütz^d, Jianlin Zhao^c, Pierre Boillat^{e,f}, Dirk Hegemann^g, René M. Rossi^b, Dominique Derome^h, Jan Carmeliet^c

^aLaboratory of Multiscale Studies in Building Physics, Empa, Swiss Federal Laboratories for Materials Science and Technology, Überlandstrasse 129, 8600 Dübendorf, Switzerland

^bLaboratory for Biomimetic Membranes and Textiles, Empa, Swiss Federal Laboratories for Materials Science and Technology, Lerchenfeldstrasse 5, 9014 St. Gallen, Switzerland

^cChair of Building Physics, Swiss Federal Institute of Technology Zurich (ETHZ), Stefano-Franscini-Platz 5, 8093 Zürich, Switzerland

^dSwiss Light Source, Paul Scherrer Institut, 5232 Villigen PSI, Switzerland

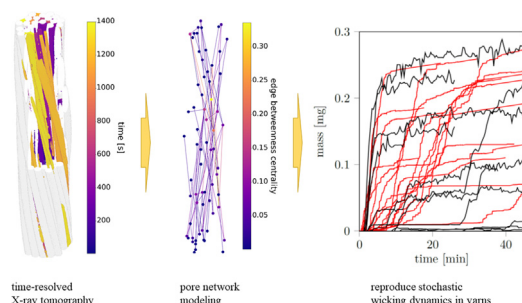
^eElectrochemistry Laboratory (LEC), Paul Scherrer Institut, 5232 Villigen PSI, Switzerland

^fLaboratory for Neutron Scattering and Imaging (LNS), Paul Scherrer Institut, 5232 Villigen PSI, Switzerland

^gAdvanced Fibers, Empa, Swiss Federal Laboratories for Materials Science and Technology, 9014 St.Gallen, Switzerland

^hDepartment of Civil and Building Engineering, Université de Sherbrooke, J1K 2R1 Sherbrooke, Canada

GRAPHICAL ABSTRACT



ARTICLE INFO

Article history:

Received 12 November 2021

Revised 8 April 2022

Accepted 9 April 2022

Available online 16 April 2022

Keywords:

X-ray tomography

Neutron radiography

Wicking

Yarn

Textile

Pore network

Spontaneous imbibition

ABSTRACT

The spontaneous imbibition of a liquid within porous media, known as wicking, can display uncommon features in textiles and yarns. Yarns exhibited step-wise wicking dynamics not captured by current models.

Hypothesis: Wicking dynamics in yarns not only depend on inter-fiber pore filling, but are mainly determined by the pore-to-pore transition processes and the structure of the pore network.

Experiments: Fast X-ray tomographic microscopy is employed to reveal the pore scale processes and neutron radiography for the macroscopic water uptake in yarns. A semi-empirical pore network model is presented that employs the measured pore network topology and pore scale dynamics to reproduce the experimentally observed wicking dynamics in yarns.

Findings: The yarn pore system is a sparse network of long and narrow pores that promotes step-wise uptake dynamics. Wicking in yarns displays fast pore filling events in the order of seconds and long waiting times between filling events up to several minutes while navigating the pore network. As main result, we find that a few filling events directly determine the macroscopic behavior of wicking in the sparse pore network of yarns. It is necessary to consider pore-to-pore transition waiting times and the pore network structure to explain the characteristics of wicking dynamics in yarns.

© 2022 The Authors. Published by Elsevier Inc. This is an open access article under the CC BY license (<http://creativecommons.org/licenses/by/4.0/>).

* Corresponding author.

E-mail address: robert.fischer@empa.ch (R. Fischer).

1. Introduction

Textiles are ubiquitous in society as clothing under a wide range of requirements and in medical and hygienic care, but also in architecture, engineering and many industrial applications. Wicking is the spontaneous imbibition of a wetting liquid into a porous medium by capillary action. Often, controlled liquid wicking is crucial or at least desirable, e.g. moisture management in functional clothing or production of fiber-reinforced materials. However, the understanding of wicking in textiles is still limited partly due to the complex inter-fibrous structure of angular, long and narrow pores. A basic framework exists since long to understand transport in generic porous media. Lucas [1] and Washburn [2] derived the dynamics of capillary rise in a circular tube as representative model. The resulting Washburn law (1) shows a square root ($b = 0.5$) function over time determined by a hydraulic radius r which is supposed to represent the average pore size [3].

$$h(t) = \sqrt{\frac{\gamma r \cos \vartheta}{2\eta} t} = Kt^b \quad (1)$$

γ is the surface tension of water in air, ϑ Young's contact angle and η the dynamic viscosity. Progress in experimental methods to determine porous structure raise doubts on this dependence on hydraulic radius which may not scale with the actual pore size in real porous media [4,5]. This issue is sometimes addressed by introducing a tortuosity-type correction factor [6,7]. Cai et al. [8] or Patro et al. [9] refined the Washburn model by allowing variable capillary shapes and sizes. However, some materials, especially textiles, are found to not obey the square root of time law at all [10,11], showing exponents b in the range of 0.16 to 0.74 [11]. Furthermore, Nyoni et al. [12] describe a large unsaturated zone instead of a sharp waterfront contradicting the assumed saturated capillary rise in Washburn-type models. Darcy-type models, e.g. with Richard's expansion [13] can accommodate partial saturation of the porous medium [14,15], but can only describe continuous wicking flow. Rather than a smooth and continuous uptake, step-wise dynamics with spatially and temporally strongly varying capillary pressure have been observed [16]. Therefore, a square-root over time behavior is not necessarily true for wicking in the particular pore space of yarns. Fitting these models with free parameters would entail pore sizes in an unphysical sub-nanometer range (see supplementary section).

Another mean to capture transport in porous media is through pore network models. Despite their simplification, pore network models can be an effective method to simulate many two-phase flow phenomena in porous media, e.g. fingering pattern [17], macroscopic pressure distributions [18] and moisture hysteresis [19], because they connect pore scale processes with the macroscales and can recover the square-root law for homogeneous porous media [20]. The challenge for network models to be an effective alternative in modeling yarn wicking lays in the identification, characterization and eventually approximation of the most relevant phenomena on both pore- and macroscale, which is still limited for spontaneous imbibition in yarns.

Thus, the need for experimental documentation at pore scale has emerged. Parada et al. [21] reviewed experimental techniques to measure wicking primarily in textiles. Neutron radiography due to its high sensitivity to hydrogen presents a particularly accurate method to quantify the time-resolved moisture distribution in porous media [22–24] and was successfully applied to textiles [14,11,25,26], but its spatial resolution and limitation to two-dimensional projection still cannot capture the processes on pore scale. Recent developments in time-resolved synchrotron X-ray tomographic microscopy (XTM) allow the study of the pore scale processes during two-phase flow in porous media [27–32]. Due to the brilliant and high intensity X-ray beam produced by a syn-

chrotron source, full microtomographic scans can be acquired in high frequency effectively providing four-dimensional information of the liquid movement inside the pore space. Parada et al. [32] demonstrated the applicability to wicking in yarns. A major leap in terms of image quality for dynamic XTM was the design and build of an advanced lens system, presented in reference [33], finally allowing to capture water wetting in yarn pores in unprecedented accuracy in space and time.

The aim of this study is to understand the wicking dynamics in yarns and its uncommon features by carefully examining the pore scale processes in textile yarns. Dynamic pore network modeling (DPNM) allows us to incorporate these two aspects and apply them to an extrapolated larger yarn domain where this pore information is not experimentally available. We will discuss how the pore wicking dynamics directly translate to overall yarn wicking dynamics.

The experimental imaging methods to study wicking dynamics on millimeter scale with accessible pore dynamics and on macroscopic centimeter scale are presented. Our previous study [16] investigated filling processes inside single yarn pores. Here, we want to focus on the wicking dynamics in an entire yarn as a network of many pores. Wicking in 29 yarn samples is studied with fast synchrotron X-ray tomography for the millimeter scale and 36 samples by neutron radiography on centimeter scale. Then, we outline a dynamic pore network model to include the pore wicking dynamics characteristic for yarns. Analysis of the experimental results provides detailed insight into the yarn wicking dynamics on the different scales with the most relevant processes and quantitative input for the model. Finally, the model is compared to the observed wicking dynamics and its applicability and limitation are discussed. We end with discussion and conclusion including the need for further research.

2. Methods

2.1. Materials

Circular polyethylene terephthalate filaments, of 55 μm diameter, are surface treated with plasma-enhanced chemical vapor deposition to ensure constant wettability at a contact angle of 48° with water owing to an ultrathin C:H:O plasma polymer layer [16]. Bundles of 32 pretreated filaments are twisted under different tension values (2.5, 10 and 30 mN/tex, where 1 tex = 1 g/1000 m) in a twist tester to yield yarns of 200 twists per meter (tpm). For the X-ray tomography, the bundles are threaded into the custom sample holders before twisting and the applied mechanical state is preserved by fixing the yarns to the sample holders using glue. The sample holder consists of two aluminum caps holding the yarn at both ends of a Kapton tube. The holder is then placed in a custom aluminum cup that acts as reservoir. A detailed description of the sample preparation can be found in [16]. A total of 29 samples was examined with 9, 10 and 10 repeats for the respective tension values 2.5, 10 and 30 mN/tex. For the neutron radiography, yarns of 32 filaments are twisted under the same three tensions at three twists (50, 200 and 500 tpm). In total, 36 samples were studied of which 22 showed wicking in the following parameter combinations: 2x (50 tpm, 2.5 mN/tex), 2x (50 tpm, 10 mN/tex), 9x (200 tpm, 30 mN/tex), 1x (500 tpm, 2.5 mN/tex), 4x (500 tpm, 10 mN/tex), 4x (500 tpm, 30 mN/tex). The different twisting parameters are motivated by investigating potential induced structural influences on the wicking dynamics.

2.2. Synchrotron X-ray tomographic microscopy

To measure water wicking in yarns on millimeter scale, time-resolved tomographic microscopic imaging is performed at the

tomographic microscopy and coherent radiology experiments (TOMCAT) beamline of the Swiss Light Source (SLS), Paul Scherrer Institut, Villigen PSI, Switzerland [34]. The samples are placed on the rotating stage of the beamline, water is released via a remotely controlled syringe pump to the reservoir and the data acquisition started simultaneously. The high brilliance of the X-ray source at the synchrotron allows obtaining a full tomographic scan per second with a voxel size of $2.75 \mu\text{m}$ at a quality sufficient to detect reliably the three phases in presence: polymer, water and air. The possible frequency of acquisition is thus 1 Hz in the field of view capturing the bottom 3 mm of the sample.

The 3D grayscale voxel data is reconstructed [35] from the acquired and phase filtered [36] absorption images. The time series of every slice undergoes a rigid-body registration [37] to allow postprocessing. The first, dry, scan is segmented into air and polymer by employing the Weka machine learning plug-in [38] for IMAGEJ (Fiji) [39]. The grayscale time series is then masked for the pore space as the exclusion of the polymer phase within the convex hull around the fiber bundles. The transition of a given voxel in the pore space from air to water is detected as the maximum gradient of the low pass filtered gray value time series. Two main analyses are performed from these time series: total volume of water in the yarn versus time and flux of water versus time. Also, to analyze pore processes, the pore space is segmented in pore bodies by a restricted watershed algorithm [40] which are then masked by the water configuration at the last time step yielding the configuration of water within the pore space versus time, from which pore scale filling events and waiting time before filling can be identified. Given the segmented data set, water volume versus time in the field of view, per pore or per height can be extracted by counting the number of voxels labeled as water per time step. Image processing and post-processing are performed using standard Python libraries (numpy, scikit-image, xarray) in an automated protocol for all samples without changes. There are no differences in image quality between samples. Image visualization is done by employing Avizo.

2.3. Neutron radiography

The neutron radiography data is obtained during the same campaign that concerned wicking in electro-spun membranes and the experiment is also described therein [41]. To measure water wicking in yarns on centimeter scale, neutron radiography imaging is performed at the Imaging with COld Neutrons (ICON) [42] beamline of the Swiss Spallation Neutron Source (SINQ), PSI, Villigen, Switzerland. Water uptake is imaged using the same three types of yarns used in X-ray tomography plus yarns at two additional twists (50 and 500 tpm). Instead of the sample holders used for XTM, the yarn samples are mounted side by side and glued in an aluminum frame allowing eight samples to be measured at once in the field of view (FOV) of $7 \times 7 \text{ cm}$. The frame is then hanged in our custom setup for neutron radiography. The procedure and setup also described in detail in [41]. Conceptually, the scattering of cold neutrons by the hydrogen nuclei of water is exploited to quantify the moisture content in a sample placed in the neutron beam, yielding a two-dimensional radiograph. Neutrons transmitted by the sample excite a $20 \mu\text{m}$ Gadox powder scintillator to emit visible light. The scintillator image is magnified by a microscope (Makro-Planar 2/100 ZF.2 T*, Zeiss, Oberkochen, Germany) and recorded by a 2048×2048 CCD-chip in a camera (iKon-L, Andor, Belfast, Northern Ireland) as 16bit-grayscale images. The acquisition is optimized to 20 s illumination time and $33 \mu\text{m}$ pixel size to achieve a sufficient signal-to-noise-ratio. To correct for detector heterogeneities, 5 images are recorded as dark current images with closed beam shutters prior to the experiment. Then, water is brought in contact with the yarns by flooding the reservoir and

images are recorded until no change in image intensity is detected (approx. 1 h).

To obtain moisture profiles in yarns, the following image processing steps are applied: Firstly, the default median filter in the Fiji distribution of ImageJ [39] replaces pixel grayvalues deviating by more than 250 from the median of its surrounding (radius = 2.5 pixel) with this median. All other processing steps are implemented in Python. A 3D-(2 space, 1 time)-Gaussian blur reduces high frequency noise ($\sigma = 0.75$ pixel), before subtracting the dark current error. The Lambert-Beer law (equation 2) can be applied pixel-wise on the dataset to obtain the time-resolved moisture maps w with water density $\rho = 997 \text{ kg/m}^3$ and attenuation coefficient $\Sigma = 470 \text{ m}^{-1}$ for the chosen scintillator-camera-combination. The mean of the initial absorption images of the dry sample is taken to obtain the reference intensity I_0 . All acquired absorption images I are then divided by I_0 .

$$I(x, y, t) = I_0(x, y) e^{-\Sigma z(x, y, t)} \quad (2a)$$

$$w(x, y, t) = \rho z(x, y, t) \quad (2b)$$

Due to the low signal-to-noise ratio, the yarn moisture profiles are obtained directly from the filtered absorption signal ratio $p(y, t) = I(y, t)/I_0(y)$ profiles. The yarn diameter is approximately $300\text{--}400 \mu\text{m}$ (≈ 10 pixels). Therefore, in a band of 40 pixels width certainly encompassing the yarn, the median of the 10 most absorbing pixels per height inside this band (location of the yarn) is taken to calculate the moisture profiles. This procedure is robust against slight variations of the yarn orientation. The profile is then smoothed by a Lowess filter over the height. A 3×3 grid of high neutron absorbing dots is placed in the FOV as a zero reference for scattering correction. However, the reference dots are too few to interpolate and reproduce the setup specific scattering errors. Therefore, the correction for the complex errors stemming from scattering in the reservoir and varying yarn diameter is approximated by referencing the absorption ratio profiles to the distorted profile of the dry yarn which would obey under ideal circumstances $p(y, t = 0) \equiv 1$.

$$p(y, t) = \frac{I(y, t)}{I_0(y)} \quad (3a)$$

$$p_{\text{corr}}(y, t) = p(y, t) - p(y, 0) + 1 \quad (3b)$$

$$p_{\text{corr}}(y, t) = e^{-\Sigma z(y, t)} \quad (3c)$$

Eqs. (3c) and (2b) can then be used to get the moisture profile in yarns in kg/m^2 . Integrating the moisture profile over the yarn width gives the uptaken water mass.

2.4. Dynamic pore network simulation

A dynamic single phase pore network model (DPNM) is employed to better understand the interaction of pore scale processes with the global yarn pore structure. The network is extracted from the segmented pore space in the image data and the simulation runs on an active sub-network, i.e. the inlets, unsaturated pores at the waterfront and filled pores behind the front. The simulation starts from filled inlet pores whose neighbors are assigned to the initial waterfront. The pressure in the inlets is set to the atmospheric pressure while the capillary pressure in the waterfront pores is known with the surface tension γ and contact angle ϑ as

$$p_i = \begin{cases} p_{\text{atm}}, & \text{for } i \in \text{inlets} \\ p_{\text{atm}} + \frac{2\gamma \cos \vartheta}{r_i}, & \text{for } i \in \text{waterfront} \end{cases} \quad (4)$$

The pores are approximated as cylindrical tubes whose radii r_i are the equivalent radii of the pores' median cross-sectional areas and

whose heights h_{oi} are calculated from the pore volume V_i occupied by water at the end of acquisition

$$h_{oi} = \frac{V_i}{\pi r_i^2} \quad (5)$$

The change of the filling state in the waterfront pores is then calculated after solving the pressures and corresponding fluxes considering conservation of masses by

$$\dot{h}_i \pi r_i^2 = q_i = - \sum_j g_{ij} (p_j - p_i) \quad (6)$$

where the corresponding Hagen-Poiseuille conductivity g_{ij} of the links is

$$g_{ij} = \left(\frac{4\eta h_i(t)}{\pi r_i^4} + \frac{4\eta h_j(t)}{\pi r_j^4} \right)^{-1} \quad (7)$$

A pore that reaches its saturation height h_0 is removed from the waterfront, assigned to the filled pores and its empty neighbors are added as waterfront pores after a waiting time to the new waterfront. The waiting time takes into account the process of the meniscus passing through a pore-to-pore transition in real porous media during spontaneous imbibition. Here, the waiting times are determined empirically by direct analysis of the time-resolved image data and described in the experimental results section. The conductivity matrix g_{ij} and waterfront pressures are updated to calculate the pore pressures at the next time step.

As a result, the model is essentially a variant of the classic single-phase dynamic pore network model of steady flow, e.g. [43,44], with the addition of a moving waterfront and running on a sub-network of active pores determined by the pore filling state and an empirical waiting time. Potentially, edge effects can limit the applicability of the DPNM because water continues to rise in the experiment outside of the FOV while the yarn inside the FOV is not yet saturated. In the model, water can only advance inside the provided pore network, but not beyond. The description of the DPNM is extended in the supplementary material. The model is implemented in Python using numpy.

3. Results

The results section contains the most important findings. Additional supportive, yet optional for the analysis, information is found in the supplementary material section.

3.1. Static XTM and network structure

The 29 segmented tomographs are postprocessed to document their pore systems. Fig. 1 shows the fibrous structure obtained from XTM (Fig. 1b) next to scanning electron microscopy image (Fig. 1a) and the extracted pores (Fig. 1c,d). Generally, pore geometries are long (0.1–3 mm) and narrow (0.0001–0.003 mm²) [16]. The pore object labels in Fig. 1c,d are obtained by applying a restricted watershed algorithm [40] on the convex hull around the segmented fibers [16]. The pore network is then created by establishing a link between pore objects that are in contact, i.e. when differently labeled pixels are in contact in the image data. The obtained network of connected pores yields topological information on the numbers of pores, connectivity and edge betweenness centrality. The networks are small with less than 100 nodes on average in the field of view (FOV). For most pores, the connectivity is small with the distribution peaking at three connected neighbors. High values rapidly become less probable, but can count up to 20 neighbors for some pores. It is difficult to judge if not spurious pixels, either image or pore segmentation errors, have been

falsely labeled as separate pores and are yielding those few high values. Edge betweenness centrality is an additional measure for the network connectivity and hierarchy; it counts the number of shortest paths between any two nodes that go through a certain link. Higher values for links between pores indicate that they are included in more shortest paths between any pair of nodes. Removing such links increases the probability to split the network into separate clusters [45]. Newman and Girvan [46] refined the evaluation of high centrality links by iteratively removing the link with highest centrality (most valuable edge, MVE) and recalculating the centralities of the remaining network. We define the edge betweenness centrality as the maximum of the edge betweenness centrality after removing five times the MVE. While breaking up the algorithm after five iterations is purely arbitrary, we find that most networks haven't fallen apart by then and the subsequently obtained centrality measures show no relation to the flow dynamics. Links with high edge betweenness centrality act as hubs and are of crucial importance for the network navigability. Some links have a centrality approaching 0.5 indicating that half of the shortest paths run through this link. While our earlier work [16] is concerned about the processes inside the pores themselves, the main interest here is wicking in the entire network of pores. The porosity, defined as the void fraction of the volume delimited by the convex hull around the dry fibers, is presented in Fig. 2a) for all samples. Most samples, regardless of their tension, have a porosity of roughly 0.3. Porosity decreases slightly and shows less spread with higher tension. Fig. 2b) shows the pore volume distributions per applied tension value as obtained from the pore segmentation. The pore volume distribution are similar where the samples with 10 mN/tex show a little higher prevalence for medium sized pores ($\approx 10^{-5}$ mm³). However, due to the high geometrical anisotropy with pores stretching across the entire FOV and since mostly less than 100 pores are captured per sample, there is no guarantee that the pore volume distributions and porosities are statistically representative for the yarn at a length of more than a few millimeters. Overall, the tested variation of tension values appears to have little influence on typical macroscopic pore characteristics.

3.2. Dynamic XTM and neutron radiography

Visual inspection of the image data showed no signs of fiber movement and evaporation effects are found to be negligible in a first order analysis at least for the early stage of the measurement given the compact yarn structure. The amount of uptaken water versus time is presented in Fig. 3 for all measurements that showed wicking during the XTM experiments. Not shown are samples and runs that did not wick at all, this includes equally many samples of each tension value and even repeats of the same sample. Most notable is the wide spread of the dynamic uptake behavior between all samples regardless of their mechanical state. The variability between repeats of the same tension is larger than among tension values. No obvious connection can be drawn from the minor differences in macroscopic pore properties (Fig. 2) and the high variability of uptake dynamics (Fig. 3). All clearly deviate from the square-root behavior. Attempting to fit the mean uptake curve to Washburn's law (8) results in an unreasonable hydraulic radius r of 138 pm. Beyond the spread of individual uptake curves, wicking dynamics in yarns are too slow to be explained by (8).

$$V(t) = Ah(t) = A \sqrt{\frac{r\gamma \cos \vartheta t}{2\eta}} \quad (8)$$

V is the uptaken water volume, A the porous cross section area, h the uptake height, γ the surface tension of water in air, ϑ the contact angle of water on the solid PET and η the dynamic viscosity of water.

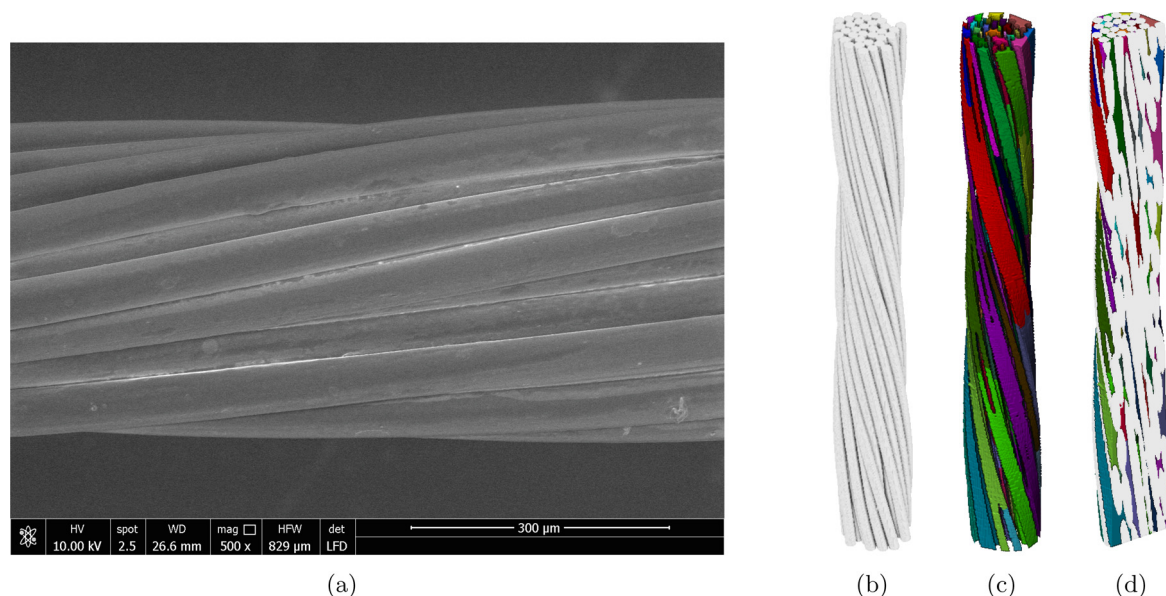


Fig. 1. (a) Scanning electron microscopy of assembled yarn. 3.3 mm high, three-dimensional orthographic visualization of dry XTM-data: (b) fibers, (c) extracted pores, (d) cut with fibers and pores. Sample: 10 mN/tex 10/III.

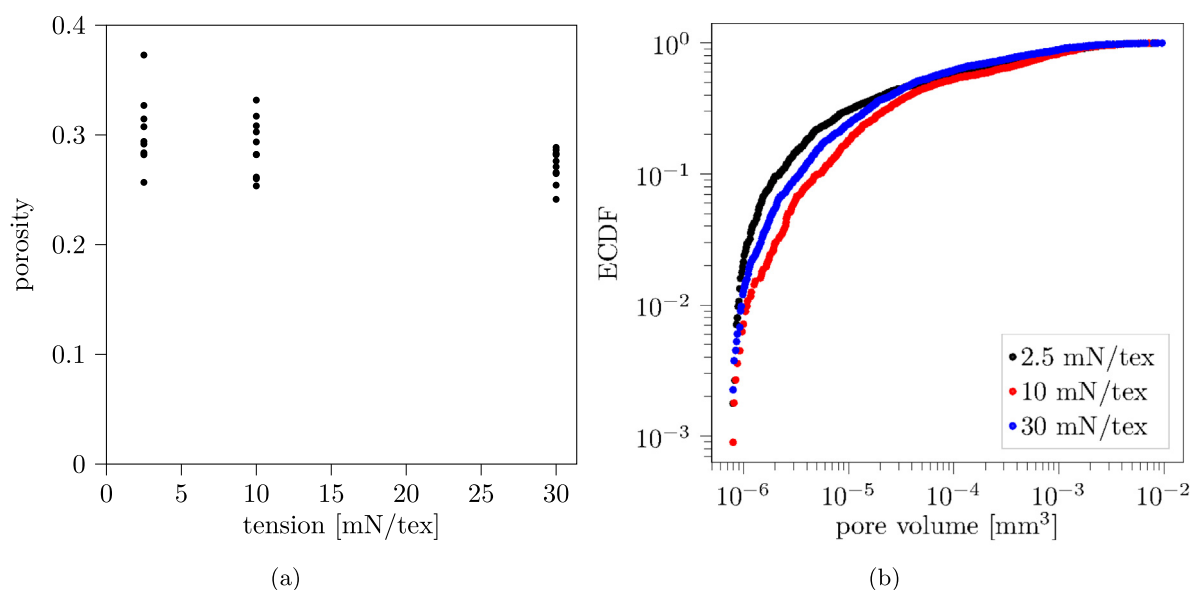


Fig. 2. (a) Porosity versus tension for all samples. (b) Pore volume distribution per tension value.

In several samples, especially those twisted under low tension (2.5 mN/tex, black), water rises significantly only after a waiting time in the order of minutes. Not only the dynamics, but also the total final amount of water greatly differs across samples. However, all samples display a step-wise uptake. This step-wise behavior is examined in detail. Fig. 4 displays the water configuration for selected time steps, where colors denote the arrival time of water at the given location. The entire time series is presented in supplementary movie 1. Already at an early stage (Fig. 4a), thin corner films can be observed with water present over the total height of the three yarns and is likely continuing to rise above the FOV. The steps observed in Fig. 3 do not manifest themselves as step-wise advancing saturation front along the height direction, but rather as filling of large sub-volumes seemingly arbitrarily distributed along the yarn length. Water content increases in different limited yarn segments in rapid, almost simultaneous filling events.

Due to the characteristic shape of yarn pores, water can be easily transported in yarn direction quickly reaching the top of the FOV (Fig. 4b,c,d). The horizontal flow between these pores is hindered and a large unsaturated zone is created by preferential vertical flow in a network of pores (Fig. 4e,f). Late filling events can also happen in the center of the FOV (Fig. 4g,h). The yarn pore structure is open to the surrounding leaving open paths for air and no air entrapment is observed. XTM is limited to a field of view of a few millimeters, but neutron radiography allows obtaining the moisture profile of the entire yarn. Fig. 5 compares the moisture profile evolution of a short (3.3 mm) yarn section as obtained by XTM to the profile of the entire yarn of 40 mm measured with NR. If it were possible to perform XTM and NR on the same sample, the entire XTM-profile would correspond to the first 3.3 mm of the NR-profile. Overall, the final moisture profile of the whole yarn is characterized by a saturated zone of uniform moisture content

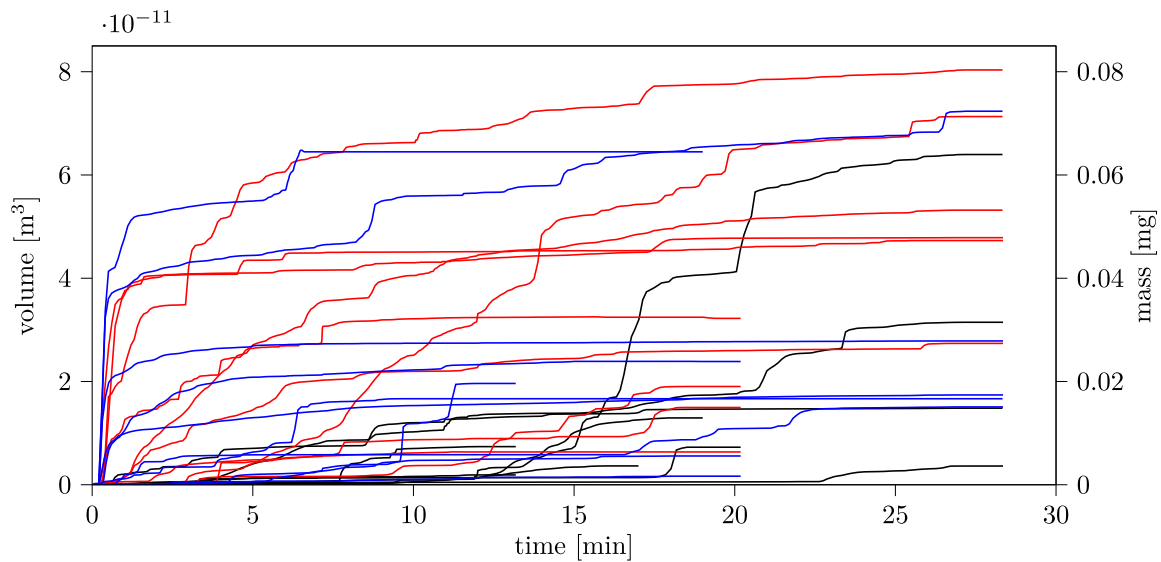


Fig. 3. Total water volume in XTM FOV versus time. Black, red and blue represent yarn samples spun under applied tension of 2.5, 10, and 30 mN/tex.

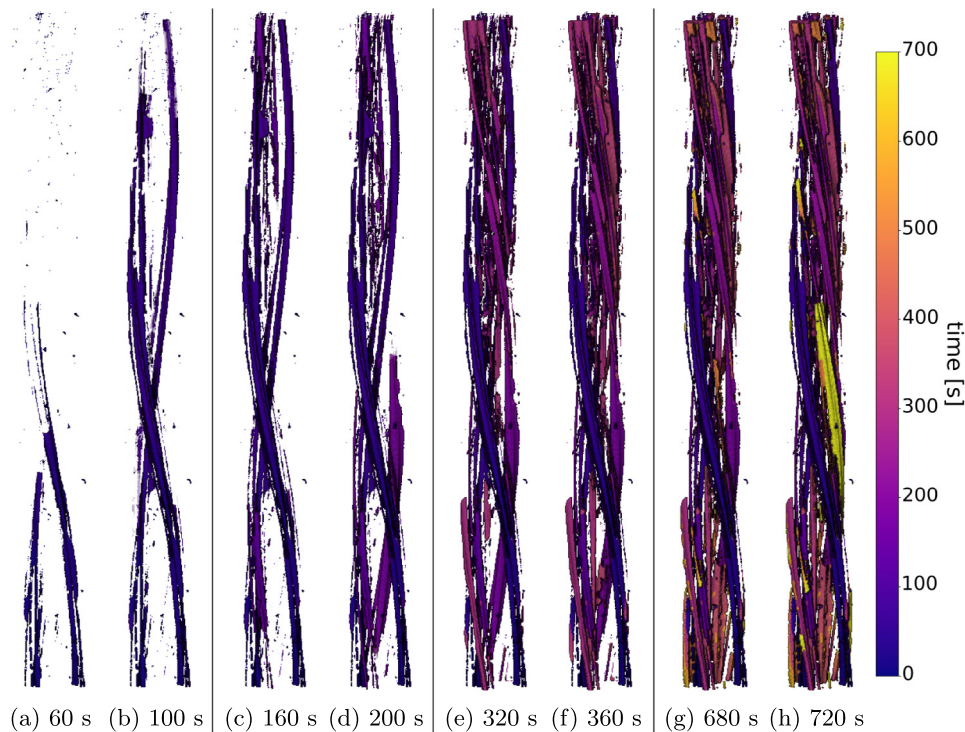


Fig. 4. Orthographic 3D-Visualization of water in yarn over time highlighting the water configuration before and after high flux peaks. Water arrival is given as color with the colorbar as reference. Sample: 7/III 10 mN/tex. The displayed height is 3.3 mm. Also shown in supplementary movie 1.

approximately 10 mm from the bottom and an unsaturated zone with decreasing moisture content with increasing height until a height of approximately 30 mm where potentially present water content can no longer be distinguished from noise. Looking at the dynamics, similarly to what is observed on millimeter scale (Fig. 5a), water advances over large distances up to centimeters in sub-volumes without saturating the yarn, resulting in the moisture profile evolution in Fig. 5b. The unsteady spacing and shape of the subsequent profiles in Fig. 5a) are also seen in Fig. 5b), e.g. at height 15 mm, with similar profiles for sustained periods of time and drastic changes of profile shape over time.

This data corroborates that the transport occurs in a series of bursts although only the most prominent burst can be resolved on the scale of the NR experiment. The described step-wise uptake behavior is not limited to negligible local processes, but characteristic for this porous medium as it can be observed not only on sub-millimeter but also on macroscopic centimeter scale. The total uptaken water mass obtained from the neutron radiographs is shown in Fig. 6. Due to the limited spatial and temporal resolution of these measurements, only the prominent steps can be resolved on this scale. Also on centimeter scale, the variability between measurements of the same yarn variable is far greater than

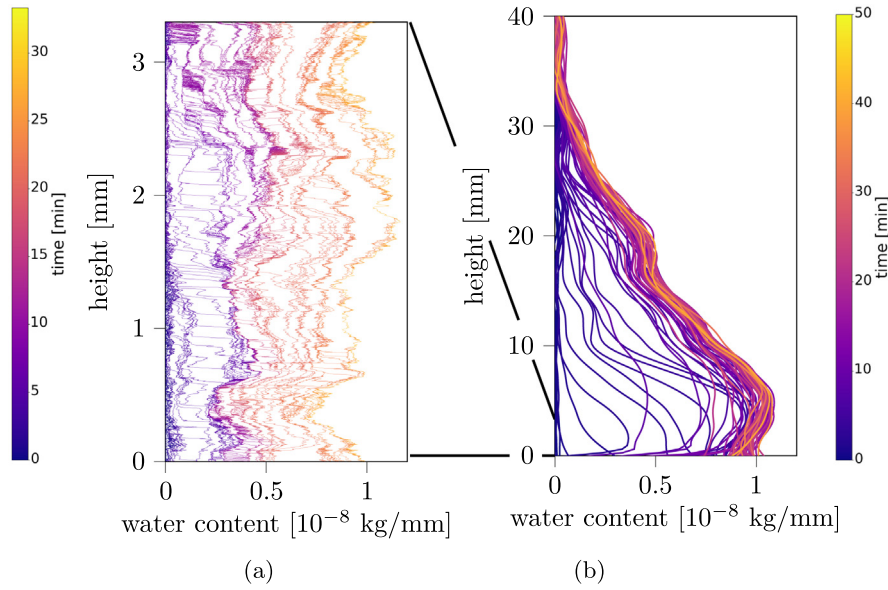


Fig. 5. (a) exemplary moisture profile obtained by XTM (sample 2.5 mN/tex 3/III) compared to (b) a moisture profile obtained by NR (sample 30 mN/tex, 200 tpm, yarn 5).

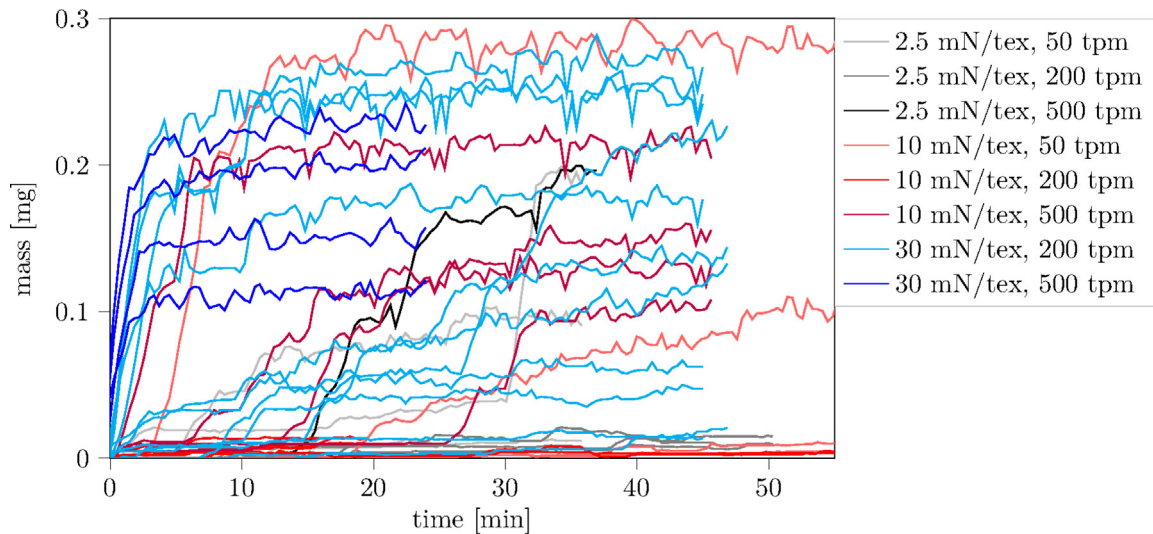


Fig. 6. Total uptaken mass over time in yarns measured with neutron radiography.

between different yarn variables. The tested yarn variables appear to be too similar to have any substantial influence on the wicking dynamics. The irregular yarn wicking dynamics measured by NR are directly influenced by pore filling processes observed by XTM and the dynamic pore scale behavior is further analyzed. In opposition to the overall slow, minute-long and step-wise wicking process in the full yarn, capillary rise in one pore happens mostly as one smooth and fast transition from dry to wet in the order of seconds. These transitions are detected as peaks in the per pore volume flux curve. As in our previous work on the pore dynamics [16], a peak is defined as any local flux maximum that is at least 7 s away from the next higher peak (temporal resolution), has a prominence of at least $75 \text{ voxel/s} \approx 1.6 \cdot 10^{-6} \text{ mm}^3/\text{s}$ and exceeds $150 \text{ voxel/s} \approx 3.1 \cdot 10^{-6} \text{ mm}^3/\text{s}$. The water volume versus time transition itself is best fitted as sigmoidal transition (equation 9a) to the pore water volume over time giving generally good agreement as indicated by R^2 close to one for most pores. The few instances of $R^2 = 0$ are mostly pores that remain empty or con-

tain image processing artifacts. Super-posing all the per pore body sigmoidal fillings (equation 9) by $V_{\text{yarn}}(t) = \sum_k V_k(t)$ recovers closely the uptake process in the full yarn (Figs. 7). Wicking in the studied yarns is therefore a series of rapid pore filling events where the most relevant parameter is the moment of filling (t_{0k} in equation 9)) and α_k the finally uptake volume in m^3 of each pore. The shape factor β_k has the unit s^{-1} and is related to the slope at $t = t_{0k}$ as seen by first order Taylor approximation (equation 9b). $\alpha_k \beta_k$ has consequentially the units of a flow rate $\text{m}^3 \text{s}^{-1}$. However, β_k is less relevant in view of the almost instantaneous pore filling compared to the slower yarn wicking dynamics.

$$V_k(t) = \frac{\alpha_k}{1 + e^{-\beta_k(t-t_{0k})}} \quad (9a)$$

$$V_k(t) \approx \alpha_k \left(\frac{1}{2} + \frac{\beta_k(t-t_{0k})}{4} \right) \quad (9b)$$

While the pore filling is fast, there can be a substantial time interval before the filling of the next pore begins. This waiting interval can

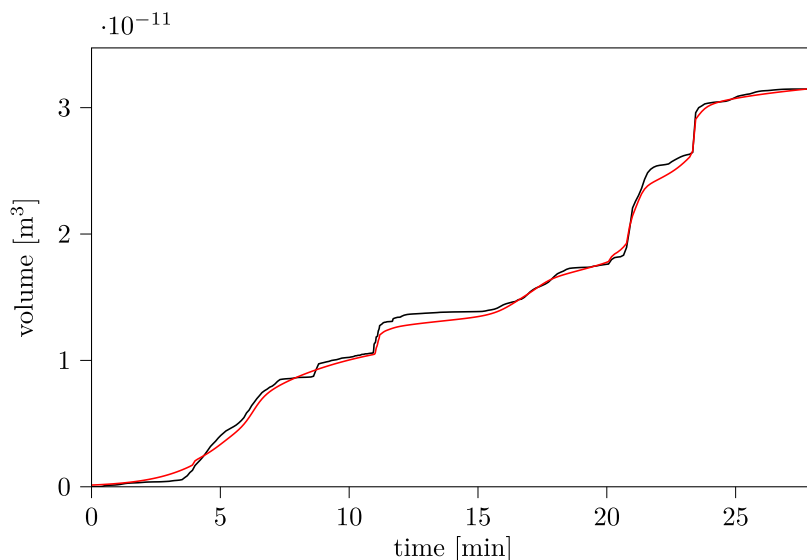


Fig. 7. Total XTM experimental uptake in black and fit of super-posed sigmoidal per-pore filling events (red) for a representative yarn sample (2.5 mN/tex 3/III). (For interpretation of the references to colour in this figure legend, the reader is referred to the web version of this article.)

occur between two pores or in few cases within the same pore and is measured as the distance between peaks. The duration of these waiting times spreads over two orders of magnitudes with maximal values in the range of 1000 s.

3.3. Semi-empirical dynamic pore network model

The experimental data with the good fit as superposed per-pore sigmoidal transitions indicates that wicking in yarns happens as propagation through a sparse (low connectivity) network of long and narrow pores with waiting times between propagation steps. This behavior is simulated by the semi-empirical network described in Section 2.4. Suggested by the high variability of the experimental results, the DPNM simulation is repeated 512 times with stochastic parameter input. For each run, a sample is randomly chosen from the experimental data set. Each sample has a pore network extracted from the image data and a waiting time distribution. For each run, two pores are randomly selected as inlets and random waiting times are assigned to all pores according to the given waiting time probability distribution. The inlet resistance is estimated to $4 \cdot 10^{17}$ Pa s/m³ based on our previous study [16]. While the time instant of pore filling is the most relevant parameter, the correct calculation of the pore filling rate itself by the DPNM is still necessary because there are few slow pore filling events that are in the range of the inter-pore filling waiting times.

Given this input, the yarn water uptake simulation statistics are compared to the experiments in Fig. 8. The supplementary material section contains an extended overview of the simulation results. Selected simulation runs show uptake characteristics comparable to the different experimental samples. The step-wise dynamics are recovered, arguably more pronounced in the simulation than in the slightly smoother experimental curves with more round edges. The reason for that can be twofold. Firstly, the limited temporal resolution of the experiment can blur sharp water volume changes that are resolved in the DPNM as demonstrated with the experimental cutoff for the maximal detectable pore flux. Secondly, the approximations in the pore network model that simplifies experimental low fluxes like corner flows (e.g. Fig. 4a), small water interface re-configurations [16] and multiple filling steps per pore and amalgamates them into one pore-to-pore transition

waiting time with a complete arrest of the water with no flux result in a more pronounced step-wise behavior.

A substantial number of simulation runs does not reach saturation due to assigned waiting times delaying the activation of pore fillings until after the investigated time interval. This falls in line with the experimental observation where some samples are not reaching saturation during the acquisition time. Overall, the model captures the experimentally observed wicking dynamics in yarns by a comparable mean uptake curve and similar uncertainty (Fig. 8a). While every experimental repeat and simulation run shows a very distinct uptake curve, the average uptake dynamics including its variance can be recovered. The model also captures well the extremes of almost instantaneous uptake and virtually no water wicking. The qualitative and quantitative similarity of the moisture profile evolution on millimeter (XTM) and centimeter scale (NR) in the limit of the lower spatial and temporal resolution of NR encourages the upscaling of the current DPNM on mm scale to yarn on macroscale (cm) using the empirical pore scale information. To obtain a network representing a yarn of 3.3 cm length, 10 networks are randomly chosen among the different yarns of the XTM data set, stacked and stitched by aggregating the pores found in the top and respectively bottom tomographic slice (Fig. 8b,c). As before, two random inlets are chosen in the lowest network and random waiting times are assigned based on the experimental waiting time distribution corresponding to the yarn selected for the lowest network. Fig. 8d) compares the uptake curves for yarns by NR and 64 simulation runs on the extrapolated centimeter scale. The mean uptake with its standard deviation is plotted for both experiment and simulation for the predominant acquisition period of 45 min. A good quantitative match and similar uptake dynamics are achieved for both individual and mean uptake curves. In few cases, a rapid initial filling is observed experimentally on millimeter and centimeter scales. The model fails to capture this behavior in the same strong manner on both scales leading to a slower mean uptake curve at early times for the simulation compared to the experiments.

4. Discussion

Time resolved three-dimensional imaging reveals the particular pore space of yarns and pore network structure. The temporal

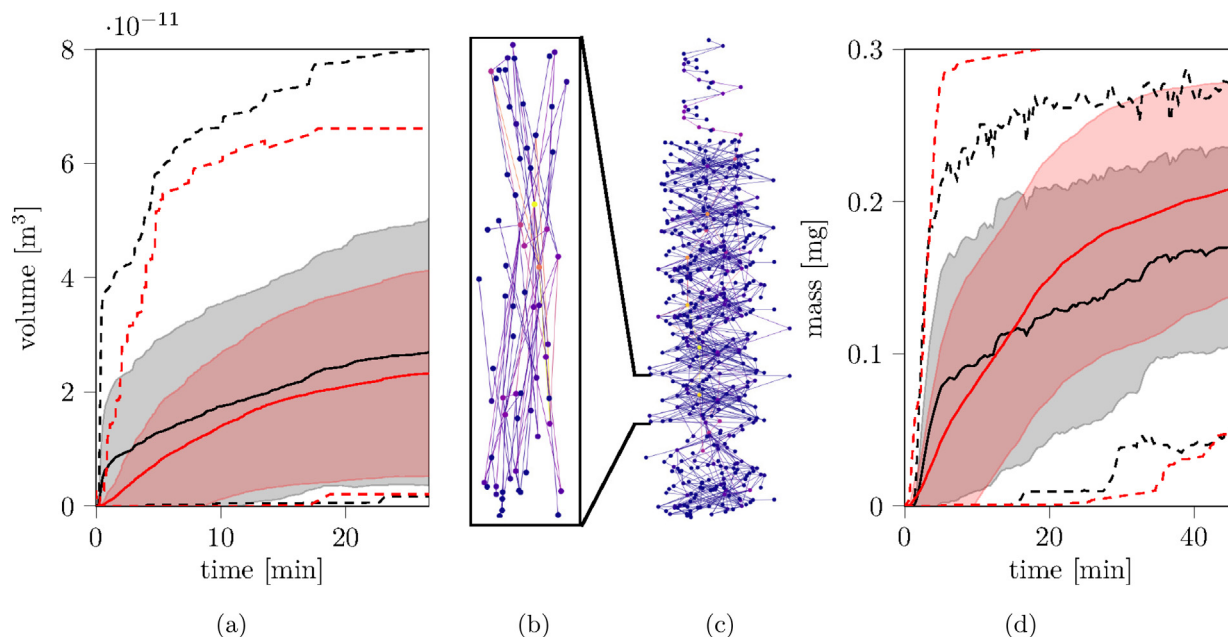


Fig. 8. (a) Statistical comparison of experiment (black) to simulation (red) at the size of the XTM FOV. (b) display of pore network, (c) 10x stacked network for up-scaling (d) comparison of up-scaled DPNM to NR experiments. The solid lines are the average uptake curves. The gray and red areas outline the standard deviations of the mean curves. The dashed lines depict the maxima and minima found.

information of water distribution shows that the network of long and narrow pores promotes an irregular wicking behavior with preferential flow along the yarn axis advancing water far ahead before eventually saturating the pore space behind the water furthest ahead. The consequence is a long unsaturated zone instead of a sharp waterfront observed typically for spontaneous imbibition in porous media. The pore structure also affects the dynamics of the capillary rise. While pore filling events are fast and move up large amounts of water into the slender pores, the pore to pore transition can take a long time. We have studied the origins of these waiting times in our previous study [16]. An unfavorable free energy evolution leads to very slow wicking fluxes inside quasi-equilibria resulting in waiting times between rapid pore filling events. Effectively, the capillary pressure that moves the liquid interfaces depends on the, potentially vanishing, balance of creating water/air interface that requires work and wetting solid surface, which provides energy. The question is not conclusively solved, but there are strong indications that the waiting times follow a common and reliable stochastic distribution. The horizontal connectivity, i.e. connection between pores at the same height, is low and the availability of alternative network percolation paths is limited as denoted by the generally low pore connectivity and betweenness centrality. Additionally, the yarn geometry and connectivity is anisotropic leading to preferred paths in the direction of the yarn axis.

Consequently, wicking in yarns is the propagation of water through a sparse network in a series of steps and voids the assumption necessary to apply Washburn's law with one representative hydraulic radius. The per-pore sigmoidal fits demonstrate by closely recovering the macroscopic wicking dynamics that this network propagation corresponds to two step types: fast filling of pores (node transitions) and slow pore-to-pore transitions at links. It is necessary to consider the pore scale processes and their interplay in the pore network to understand the anomalous macroscopic dynamics deviating from the expected square-root law. The two experimentally observed network propagation step types are incorporated in our pore network model. The pores are approximated as tube segments for which the flow conductivity can be analytically solved and the dynamic pressure field in the pore net-

work be obtained as balance between capillary action at the front pores and pore network flow resistance by the dynamic pore network model (DPNM). The origin of the waiting time for water transitions between neighboring pores is part of ongoing research and related to variable capillary pressure [16]. There is currently no consistent understanding for this transition waiting time and the experimentally obtained distribution is used as an empirical input for the model.

In both, experiment and simulation, it is found that the fast pore filling events determine the amount of uptaken water, but are less important, while not entirely negligible, for the macroscopic wicking dynamics in view of the long waiting times at links between pores. The wicking dynamics are determined by the sequence of these pore to pore transitions and corresponding waiting times while the water navigates through a sparse pore network. Due to the limited number of alternative paths in the sparse pore network, long waiting times at certain links have a determining impact on the macroscopic dynamics. Subtle changes in the pore structure and water interface evolution can have a huge impact on the macroscopic wicking dynamics leading to the enormous variability of observed wicking dynamics. This can include almost instantaneous water uptake or none at all.

The model cannot directly predict the capillary uptake in single yarns but reproduces qualitatively the experimental dynamics and quantitatively in the statistically expected range for the investigated set of yarns. Due to the necessary experimental input to the model, the applicability is currently limited to the yarns prepared and tested for this study. The model gives a good match on the centimeter scale with using the millimeter scale XTM-data as model input. The extrapolation of the network model from millimeter to centimeter scale recovers the uptake dynamics observed on centimeter scale with NR. This shows that by understanding the pore scale processes and their interplay with the pore network topology in a small part of the pore space, the macroscopic wicking dynamics can be understood even if they show anomalous behavior. The DPNM additionally allows us to understand the stochastic nature of wicking dynamics in yarns macroscopically and provides a good approximation of the pore filling processes microscopically. Previous models that assume piston-like uptake with invariable

capillary pressure cannot capture the characteristic wicking dynamics and fitting the proposed equations leads to unrealistic pore geometry parameter (see supplementary material). The DPNM without considering the waiting times corresponds to the current employment of pore network models and neither can capture the experimental wicking dynamics.

We refrain from further extrapolation of our modified DPNM without a solid model predicting the evolution of the waiting time distribution and without consideration of gravity for larger wicking heights. The DPNM, however, has all the ingredients to include a viscous dissipation dependent waiting time model and gravitational effects in the future.

We did not observe whether macroscopic parameters describing the mechanical state (tension) of the yarn significantly translate into effective wicking parameters. There appears to be a non-trivial dependency of the yarn's mechanical state, pore network topology and the filling sequence. There is research potential to estimate the waiting time distribution based on yarn pore structure and flow resistance.

5. Conclusion

Fast X-ray tomographic microscopy is employed to capture the wicking dynamics in polyester filament yarns on inter-filament pore level and compared to macroscopic moisture distribution obtained by neutron radiography. Instead of a sharp waterfront advancing, wicking in yarns happens as series of bursts corresponding to the filling of long and narrow pores between the fibers resulting in a long unsaturated zone on the centimeter scale. Lucas-Washburn [1,2,6,8] and Darcy [14,15] type models of wicking deserve merit for their applicability to many porous media, but are unable to capture the wicking dynamics in yarns.

The dynamics of wicking in yarns is explained as a sparse network propagation with fast pore filling events and slow pore to pore transitions. Due to the small number of pores, the transitions can dominate the macroscopic wicking behavior if they link otherwise disconnected parts of the pore network by delaying the overall water uptake.

As a consequence of the stochastic nature of these delays, the variance of uptake behavior is high and can differ in the range of tens of minutes for identically prepared yarns in the presented experimental setup. The rapid pore filling is found to occur in all samples and to be characteristic for twisted filament yarns which can be demonstrated by the effective fit using a super-position of per-pore sigmoidal transitions. A new semi-empirical pore network model is developed to consider both the stochastic pore scale processes and the influence of the inter-filament pore network topology. Different to previous dynamic pore network models (DPNM) [18,43,47–50], we consider a stochastic empirical pore-to-pore transition waiting time that is not considered by typical pore scale approximations in DPNM. The pore network model captures the statistics of the experimentally observed wicking dynamics in yarns in the range of the presented experimental setting. Future work can include informing a DPNM with direct simulation, e.g. Lattice Boltzmann Method, on pore scale to directly predict the pore-to-pore transition waiting times. Eventually, with further research, the goal will be to create a virtual pore network from statistical yarn characteristics for practical applications without the need for extensive experimental work.

Declaration of Competing Interest

The authors declare that they have no known competing financial interests or personal relationships that could have appeared to influence the work reported in this paper.

Acknowledgments

We are grateful to Monosuisse AG for providing the fibers. We acknowledge Stefan Carl and Sascha Krügl for the experimental setup. We also want to thank Sascha Krügl, Mathieu Decrette and Marie-Ange Bueno for the support during the sample preparation. We further acknowledge the Paul Scherrer Institut, Villigen, Switzerland for provision of synchrotron radiation beamtime at the TOMCAT beamline X02DA of the SLS and neutron radiation beamtime at the ICON instrument of the SINQ facility. We also thank Laurent Cimon for the valuable help to optimize the code of the model implementation and Robin Pauer for the SEM. We acknowledge the helpful advice by the anonymous reviewers. This research did not receive any specific grant from funding agencies in the public, commercial, or not-for-profit sectors.

Appendix A. Supplementary material

Supplementary data associated with this article can be found, in the online version, at <https://doi.org/10.1016/j.jcis.2022.04.060>.

References

- [1] R. Lucas, *Kolloid-Zeitschrift* 23 (1) (1918) 15, <https://doi.org/10.1007/BF01461107>. URL: <https://doi.org/10.1007/BF01461107>.
- [2] E.W. Washburn, *Phys. Rev.* 17 (3) (1921) 273, <https://doi.org/10.1103/PhysRev.17.273>.
- [3] E. Kissa, *Text. Res. J.* 66 (10) (1996) 660, <https://doi.org/10.1177/004051759606601008>. URL: <Go to ISI>://WOS:A1996VK97000009 Vk970 Times Cited:174 Cited References Count:109.
- [4] D. Benavente, P. Lock, M. Angeles García Del Cura, S. Ordóñez, *Transport in Porous Media* 49(1), 59 (2002). doi:10.1023/a:1016047122877
- [5] J. Schoellkopf, P.A.C. Gane, C.J. Ridgway, G.P. Matthews, *Colloids Surf., A* 206 (2002) 445.
- [6] T. Liu, K.F. Choi, Y. Li, *J Colloid Interface Sci* 318(1), 134 (2008). doi:10.1016/j.jcis.2007.10.023. URL: <https://www.ncbi.nlm.nih.gov/pubmed/17980383> https://ac.els-cdn.com/S0021979707015123/1-s2.0-S0021979707015123-main.pdf?_tid=3891f342-d5af-11e7-bb69-00000a0f01&acdnat=1512033600_a86c32e4a40042a73160e8fd0821ae4f.
- [7] J. Cai, B. Yu, *Transp. Porous Media* 89 (2) (2011) 251, <https://doi.org/10.1007/s11242-011-9767-0>.
- [8] J. Cai, E. Perfect, C.L. Cheng, X. Hu, *Langmuir* 30(18), 5142 (2014). doi:10.1021/la5007204. URL: <https://www.ncbi.nlm.nih.gov/pubmed/24785579>. Cai, Jianchao Perfect, Edmund Cheng, Chu-Lin Hu, Xiangyun eng Langmuir. 2014 May 13;30(18):5142-51. doi: 10.1021/la5007204. Epub 2014 May 1.
- [9] D. Patro, S. Bhattacharyya, V. Jayaram, *J. Am. Ceram. Soc.* 90 (10) (2007) 3040, <https://doi.org/10.1111/j.1551-2916.2007.01776.x>.
- [10] I. Pezron, B. Bourgain, D. Quéré, *J. Colloid Interface Sci.* 173 (2) (1995) 319, <https://doi.org/10.1006/jcis.1995.1331>.
- [11] M. Parada, P. Vontobel, R.M. Rossi, D. Derome, J. Carmeliet, *Transp. Porous Media* 119 (3) (2017) 611, <https://doi.org/10.1007/s11242-017-0901-5>. URL: <Go to ISI>://WOS:000412540600006 <https://link.springer.com/content/pdf/10.1007%2Fs11242-017-0901-5.pdf>. Fj2fs Times Cited:0 Cited References Count:36.
- [12] A.B. Nyoni, D. Brook, *J. Text. Inst.* 97 (2) (2006) 119, <https://doi.org/10.1533/joti.2005.0128>.
- [13] L.A. Richards, *Physics* 1 (5) (1931) 318, <https://doi.org/10.1063/1.1745010>.
- [14] M. Parada, X. Zhou, D. Derome, R.M. Rossi, J. Carmeliet, *Text. Res. J.* (2018), <https://doi.org/10.1177/0040517518758007>.
- [15] M.A.F. Zarandi, K.M. Pillai, *AIChE J.* 64 (1) (2018) 306, <https://doi.org/10.1002/aic.15856>.
- [16] R. Fischer, C.M. Schlepütz, D. Hegemann, R.M. Rossi, D. Derome, J. Carmeliet, *Phys. Rev. E* 103 (2021) 5, <https://doi.org/10.1103/PhysRevE.103.053101>.
- [17] R. Lenormand, C. Zarcone, *Transport in Porous Media* 4(6), 599 (1989). URL: <Go to ISI>://WOS:A1989CK25000006 <https://link.springer.com/content/pdf/10.1007%2FBF00223630.pdf>. Ck250 Times Cited:51 Cited References Count:0.
- [18] J. Zhao, F. Qin, D. Derome, Q. Kang, J. Carmeliet, *Adv. Water Resour.* 145 (2020), <https://doi.org/10.1016/j.advwatres.2020.103738>.
- [19] O.E. Godínez-Brizuela, N.K. Karadimitriou, V. Joekar-Niasar, C.A. Shore, M. Oostrom, *Adv. Water Resour.* 107 (2017) 10, <https://doi.org/10.1016/j.advwatres.2017.06.007>.
- [20] C.Z. Qin, H. van Brummelen, *Adv. Water Resour.* 133 (2019), <https://doi.org/10.1016/j.advwatres.2019.103420>.
- [21] M. Parada, D. Derome, R.M. Rossi, J. Carmeliet, *Text. Res. J.* 87 (1) (2017) 110, <https://doi.org/10.1177/0040517515622151>. URL: <Go to ISI>://WOS:000390556500010. E8cr Times Cited:1 Cited References Count:83.

- [22] G. Desmarais, M.S. Gilani, P. Vontobel, J. Carmeliet, D. Derome, *Transp. Porous Media* 113 (2) (2016) 383, <https://doi.org/10.1007/s11242-016-0700-4>. URL: <Go to ISI>://WOS:000377391700007 <https://link.springer.com/content/pdf/10.1007%2Fs11242-016-0700-4.pdf>. Dn9ib Times Cited:0 Cited References Count:22.
- [23] M. Sedighi-Gilani, M. Griffa, D. Mannes, E. Lehmann, J. Carmeliet, D. Derome, *Int. J. Heat Mass Transf.* 55 (21–22) (2012) 6211, <https://doi.org/10.1016/j.ijheatmasstransfer.2012.06.045>.
- [24] J. Dewanckele, T. De Kock, G. Fronteau, H. Derluyn, P. Vontobel, M. Dierick, L. Van Hoorebeke, P. Jacobs, V. Cnudde, *Mater. Charact.* 88 (2014) 86, <https://doi.org/10.1016/j.matchar.2013.12.007>.
- [25] M. Weder, P.A. Bruhwiler, U. Herzig, R. Huber, G. Frei, E. Lehmann, *Text. Res. J.* 74 (8) (2004) 695, <https://doi.org/10.1177/004051750407400807>. URL: <Go to ISI>://WOS:000223417100007. 847tf Times Cited:11 Cited References Count:24.
- [26] F.A. Reifler, E.H. Lehmann, G. Frei, H. May, R. Rossi, *Meas. Sci. Technol.* 17 (7) (2006) 1925, <https://doi.org/10.1088/0957-0233/17/7/034>.
- [27] R. Mokso, C.M. Schlepütz, G. Theidel, H. Billich, E. Schmid, T. Celcer, G. Mikuljan, L. Sala, F. Marone, N. Schlumpf, M. Stampanoni, *J. Synchrotron Radiat* 24(Pt 6), 1250 (2017). doi:10.1107/S1600577517013522. URL: <https://www.ncbi.nlm.nih.gov/pubmed/29091068>. Mokso, Rajmund Schlepütz, Christian M Theidel, Gerd Billich, Heiner Schmid, Elmar Celcer, Tine Mikuljan, Gordan Sala, Leonardo Marone, Federica Schlumpf, Nick Stampanoni, Marco eng 2009-07/ PSI-FOKO/ J Synchrotron Radiat. 2017 Nov 1;24(Pt 6):1250-1259. doi: 10.1107/S1600577517013522. Epub 2017 Oct 17.
- [28] K. Singh, H. Menke, M. Andrew, Q. Lin, C. Rau, M.J. Blunt, B. Bijeljic, *Sci Rep* 7(1), 5192 (2017). doi:10.1038/s41598-017-05204-4. URL: <https://www.ncbi.nlm.nih.gov/pubmed/28701699>. Singh, Kamaljit Menke, Hannah Andrew, Matthew Lin, Qingyang Rau, Christoph Blunt, Martin J Bijeljic, Branko eng Research Support, Non-U.S. Gov't England Sci Rep. 2017 Jul 12;7(1):5192. doi: 10.1038/s41598-017-05204-4.
- [29] K. Singh, H. Scholl, M. Brinkmann, M.D. Michiel, M. Scheel, S. Herminghaus, R. Seemann, *Sci Rep* 7(1), 444 (2017). doi:10.1038/s41598-017-00191-y. URL: <https://www.ncbi.nlm.nih.gov/pubmed/28348395>. Singh, Kamaljit Scholl, Hagen Brinkmann, Martin Michiel, Marco Di Scheel, Mario Herminghaus, Stephan Seemann, Ralf eng Research Support, Non-U.S. Gov't England Sci Rep. 2017 Mar 27;7(1):444. doi: 10.1038/s41598-017-00191-y.
- [30] J.W. Buurlage, F. Marone, D.M. Pelt, W.J. Palenstijn, M. Stampanoni, K.J. Batenburg, C.M. Schlepütz, *Sci Rep* 9(1), 18379 (2019). doi:10.1038/s41598-019-54647-4. URL: <https://www.ncbi.nlm.nih.gov/pubmed/31804524>. Buurlage, Jan-Willem Marone, Federica Pelt, Daniel M Palenstijn, Willem Jan Stampanoni, Marco Batenburg, K Joost Schlepütz, Christian M eng 639.073.506/Nederlandse Organisatie voor Wetenschappelijk Onderzoek (Netherlands Organisation for Scientific Research) England Sci Rep. 2019 Dec 5;9(1):18379. doi: 10.1038/s41598-019-54647-4.
- [31] Y. Nagai, J. Eller, T. Hatanaka, S. Yamaguchi, S. Kato, A. Kato, F. Marone, H. Xu, F. N. Büchi, *J. Power Sources* 435 (2019), <https://doi.org/10.1016/j.jpowsour.2019.226809>.
- [32] M.Y.I. Parada, C.M. Schlepütz, R.M. Rossi, D. Derome, J. Carmeliet, *Text. Res. J.* (2019), <https://doi.org/10.1177/0040517519843461>.
- [33] M. Bührer, M. Stampanoni, X. Rochet, F. Büchi, J. Eller, F. Marone, *J. Synchrotron Radiat* 26 (Pt 4) (2019) 1161, <https://doi.org/10.1107/S1600577519004119>. URL: <https://www.ncbi.nlm.nih.gov/pubmed/31274440>.
- [34] U. Bonse, M. Stampanoni, A. Groso, A. Isenegger, G. Mikuljan, Q. Chen, A. Bertrand, S. Henein, R. Betemps, U. Frommherz, P. Böhler, D. Meister, M. Lange, R. Abela, *Trends in synchrotron-based tomographic imaging: the sls experience* (2006), <https://doi.org/10.1117/12.679497>.
- [35] F. Marone, M. Stampanoni, *J. Synchrotron Radiat* 19(Pt 6), 1029 (2012). doi:10.1107/S0909049512032864. URL: <https://www.ncbi.nlm.nih.gov/pubmed/23093766>. Marone, F Stampanoni, M eng J Synchrotron Radiat. 2012 Nov; 19(Pt 6):1029-37. doi: 10.1107/S0909049512032864. Epub 2012 Sep 1.
- [36] D. Paganin, S.C. Mayo, T.E. Gureyev, P.R. Miller, S.W. Wilkins, J. Microsc. 206 (2002) 33, <https://doi.org/10.1046/j.1365-2818.2002.01010.x>. URL: <Go to ISI>://WOS:000175227800004. 1 545qb Times Cited:877 Cited References Count:46.
- [37] P. Thévenaz, U.E. Ruttimann, M. Unser, *IEEE Trans. Image Process.* 7 (1) (1998) 27.
- [38] I. Arganda-Carreras, V. Kaynig, C. Rueden, K.W. Eliceiri, J. Schindelin, A. Cardona, H. Sebastian Seung, *Bioinformatics* 33(15), 2424 (2017). doi:10.1093/bioinformatics/btx180. URL: <https://www.ncbi.nlm.nih.gov/pubmed/28369169>. Arganda-Carreras, Ignacio Kaynig, Verena Rueden, Curtis Eliceiri, Kevin W Schindelin, Johannes Cardona, Albert Sebastian Seung, H eng England Bioinformatics. 2017 Aug 1;33(15):2424-2426. doi: 10.1093/bioinformatics/btx180.
- [39] J. Schindelin, I. Arganda-Carreras, E. Frise, V. Kaynig, M. Longair, T. Pietzsch, S. Preibisch, C. Rueden, S. Saalfeld, B. Schmid, J.Y. Tinevez, D.J. White, V. Hartenstein, K. Eliceiri, P. Tomancak, A. Cardona, *Nat Methods* 9 (7) (2012) 676, <https://doi.org/10.1038/nmeth.2019>. URL: <https://www.ncbi.nlm.nih.gov/pubmed/22743772>. Schindelin, Johannes Arganda-Carreras, Ignacio Frise, Erwin Kaynig, Verena Longair, Mark Pietzsch, Tobias Preibisch, Stephan Rueden, Curtis Saalfeld, Stephan Schmid, Benjamin Tinevez, Jean-Yves White, Daniel James Hartenstein, Volker Eliceiri, Kevin Tomancak, Pavel Cardona, Albert eng R01 GM097231/GM/NIGMS NIH HHS/ R01 NS054814/NS/NINDS NIH HHS/ RC2GM092519/GM/NIGMS NIH HHS/ Research Support, N.I.H., Extramural Research Support, Non-U.S. Gov't Nat Methods. 2012 Jun 28;9 (7):676-82. doi: 10.1038/nmeth.2019.
- [40] B. Münch, P. Gasser, L. Holzer, R. Flatt, J. Am. Ceram. Soc. 89 (8) (2006) 2586, <https://doi.org/10.1111/j.1551-2916.2006.01121.x>.
- [41] R. Fischer, P. Boillat, L. Weidenbacher, D. Derome, R.M. Rossi, J. Carmeliet, *Proceedings of the 19th World Textile Conference - Autex 2019* (2019).
- [42] A.P. Kaestner, S. Hartmann, G. Kühne, G. Frei, C. Grünzweig, L. Josic, F. Schmid, E.H. Lehmann, *Nuclear Instruments and Methods in Physics Research Section A: Accelerators, Spectrometers, Detectors and Associated Equipment* 659 (1) (2011) 387, <https://doi.org/10.1016/j.nima.2011.08.022>.
- [43] K. Vandersteen, J. Carmeliet, J. Feyen, *Transp. Porous Media* 50 (3) (2003) 197, <https://doi.org/10.1023/a:1021150732466>.
- [44] W. Song, J. Yao, D. Wang, Y. Li, H. Sun, Y. Yang, *J. Petrol. Sci. Eng.* 184 (2020), <https://doi.org/10.1016/j.petrol.2019.106506>.
- [45] M. Girvan, M.E. Newman, *Proc Natl Acad Sci U S A* 99 (12) (2002) 7821, <https://doi.org/10.1073/pnas.122653799>.
- [46] M.E. Newman, M. Girvan, *Phys Rev E Stat Nonlin Soft Matter Phys* 69(2 Pt 2), 026113 (2004). doi:10.1103/PhysRevE.69.026113. URL: <https://www.ncbi.nlm.nih.gov/pubmed/14995526>. Newman, M E J Girvan, M eng Phys Rev E Stat Nonlin Soft Matter Phys. 2004 Feb; 69(2 Pt 2):026113. doi: 10.1103/PhysRevE.69.026113. Epub 2004 Feb 26.
- [47] V. Joekar-Niasar, M. Prodanovic, D. Wildenschild, S.M. Hassanizadeh, *Water Resour. Res.* 46 (2010) 6, <https://doi.org/10.1029/2009wr008585>.
- [48] V. Joekar-Niasar, S.M. Hassanizadeh, H.K. Dahle, *J. Fluid Mech.* 655 (2010) 38, <https://doi.org/10.1017/s0022212010000704>.
- [49] P. Van Marcke, B. Verleye, J. Carmeliet, D. Roose, R. Swennen, *Transp. Porous Media* 85 (2) (2010) 451, <https://doi.org/10.1007/s11242-010-9572-1>.
- [50] J. Zhao, F. Qin, D. Derome, J. Carmeliet, *J. Hydrol.* 588 (2020), <https://doi.org/10.1016/j.jhydrol.2020.125080>.